Communications in Computational Chemistry
Commun. Comput. Chem. Vol. 8, No. 1, 63–72
doi: 10.4208/cicc.2025.306.01
Communications

Machine Learning Decoherence Time Formulas with Force-Projected Kinetic Energies for Nonadiabatic Scattering Dynamics

Cancan Shao[1,2], Rixin Xie[2], Lei Huang[2] and Linjun Wang[2,*]

[1] *School of Intelligent Manufacturing, Zhejiang Polytechnic University of Mechanical and Electrical Engineering, Hangzhou 310053, China;*

[2] *Zhejiang Key Laboratory of Excited-State Energy Conversion and Energy Storage, Department of Chemistry, Zhejiang University, Hangzhou 310058, China.*

[*] Corresponding author: ljwang@zju.edu.cn.

Received 2 Nov. 2025; Accepted (in revised version) 5 Jan. 2026

Abstract: The framework of mixed quantum-classical dynamics is promising for realizing efficient and reliable simulations of general nonadiabatic dynamics processes. In particular, the surface hopping method based on independent trajectories has attracted extensive interest over the past decades. In practical applications, however, its accuracy is often limited by the overcoherence problem. To address this limitation, we here utilize a machine learning approach to reveal the optimal decoherence time formula for high-dimensional systems and consider the kinetic energy projected along various force directions as the feature inputs. Remarkably, the obtained formula consistently distinguishes itself within the training set across four distinct descriptor spaces. The systematic benchmark confirms the high reliability of the formula based on the kinetic energy projected along the force direction of the nonactive potential energy surface. In fact, the vast majority of average population errors achieved by surface hopping with the new formula are below 0.01 and 0.02 in the investigated one- and two-dimensional systems, respectively. These results thus highlight the high performance of the new decoherence time formula in nonadiabatic scattering dynamics and demonstrate the feasibility of projecting the total kinetic energy onto a proper force direction to uncover the intricate decoherence effect in high-dimensional applications.

Key words: nonadiabatic dynamics, surface hopping, overcoherence problem, decoherence time formula, machine learning.

In chemistry, physics, biology, and materials science, many important dynamical processes (e.g., photochemical reactions [1-7] photosynthesis in plants [8-11] as well as the various electron/exciton dynamics in optoelectronic materials [12-19]) all involve the participation of multiple electronic states and exhibit strong nonadiabatic effects. As a representative mixed quantum-classical dynamics method, trajectory surface hopping is supposed to achieve a good balance between simulation accuracy and computational efficiency, making it widely used in the theoretical investigation of nonadiabatic dynamics [20-23]. One of the key advantages of trajectory surface hopping lies in its seamless integration with first-principles electronic structure calculations, thus enabling real-time and real-space simulation of complex realistic systems [24,25]. In particular, a series of related software packages have been developed and widely utilized in different application scenarios [26-33]. However, the traditional fewest switches surface hopping (FSSH) [34] still suffers from some theoretical limitations, particularly in handling the overcoherence problem of high-dimensional systems due to the classical treatment of nuclear motion [35-37].

In the past decades, extensive efforts have been devoted to addressing the challenge of overcoherence in the framework of mixed quantum-classical dynamics [35-49]. In principle, by incorporating the coupling between trajectories, robust density matrix formulations can be developed to properly describe the dynamical evolution [37,43]. However, considering the strong requirement for *ab initio* nonadiabatic dynamics simulations and complex large-scale applications, independent-trajectory-based approaches offer a more efficient and accessible alternative [21-23,44]. In the standard methodology of traditional surface hopping [34], the time evolution of each trajectory comprises four main procedures: classical nuclear dynamics, electronic wavefunction propagation, calculation of hopping probabilities, and velocity adjustment after successful surface hops. At each time step, decoherence correction can be approximately introduced through a decoherence time formula, which serves as an effective strategy to improve the accuracy while maintaining the computational efficiency [45-47]. Namely, the wavefunction coefficient of any nonactive state i (i.e., w_i) is corrected by

$$w'_{i(\neq\alpha)} = w_i \exp\left(-\Delta t/\tau_{ai}\right), \tag{1}$$

where Δt is the time-step size and τ_{ai} is the decoherence time between the active state a and a nonactive state i. Accordingly, the wavefunction coefficient of the active state a (i.e., w_a) is then reset through

$$w'_a = \frac{w_a}{|w_a|}\sqrt{1-\sum_{i\neq a}|w'_i|^2}. \tag{2}$$

In this study, we identify the optimal decoherence time formulas through a general machine learning-assisted approach, which leverages the benchmark data from fully quantum dynamics and utilizes a discrete-space optimization algorithm to adaptively tune the corresponding parameters in a large set of iteratively generated decoherence time expressions [48]. Ultimately, the decoherence time can be calculated by the descriptors and the related parameters during the nonadiabatic dynamics simulation. In our recent study, we have found a novel decoherence time formula in the form of [49]

$$\tau_{ai} = C_0 + C_1\frac{\Delta E_i}{E^{\boldsymbol{D}}_{kin}(E^{\boldsymbol{D}}_{kin}-\Delta E_i)}, \tag{3}$$

where $E^{\boldsymbol{D}}_{kin}$ represents the kinetic energy based on the nuclear momenta projected along a certain direction $\boldsymbol{D}$. Specifically, for the feature input $E^{\boldsymbol{d}_{ai}}_{kin}$, $\boldsymbol{d}_{ai}$ corresponds to the nonadiabatic coupling (NAC) vector and the parameters in Eq. (3) are calculated as C_0 = 1.0×10^5 and C_1 = 20. This machine learning decoherence time formula has demonstrated high performance in both one- and two-dimensional scattering systems. Note that phase correction [50] has been employed in all surface hopping simulations and atomic units are used throughout the present study unless otherwise specified. Besides, instantaneous decoherence correction is applied when the decoherence time is negative.

In general, one may expect whether other feature input $E^{\boldsymbol{D}}_{kin}$ with different $\boldsymbol{D}$ could also give good performance. Therefore, we study the force-projected kinetic energies here. For each trajectory, the nuclear motion is solved by the Newton equation

$$\frac{d\boldsymbol{P}}{dt} = -\nabla_{\boldsymbol{R}}E_a(\boldsymbol{R}), \tag{4}$$

where $\boldsymbol{P}$ and $E_a(\boldsymbol{R})$ are the nuclear momenta and the eigenenergy of the active state a, respectively. We may first consider $\boldsymbol{D}$ as the force on the active potential energy surface (PES) in Eq. (4), $\boldsymbol{F}_a$, which is calculated during the dynamics simulation even without adding any decoherence correction. Similarly, the force acting on a nonactive state reads

$$\boldsymbol{F}_i = -\nabla_{\boldsymbol{R}}E_i(\boldsymbol{R}). \tag{5}$$

Besides $\boldsymbol{F}_a$ and $\boldsymbol{F}_i$, we also explore the force difference, which incorporates information from both the active PES a and the nonactive PES i,

$$\Delta\boldsymbol{F}_{i(\neq a)} = -\nabla_{\boldsymbol{R}}[E_i(\boldsymbol{R}) - E_a(\boldsymbol{R})]. \tag{6}$$

Similar to those in the surface hopping method, the electronic evolution in the Ehrenfest mean field (EMF) [51] approach also follows the time-dependent Schrödinger equation, and the nuclear motion is governed by the Newton equation. The difference lies in the fact that the nuclear motion in EMF is described by

$$\frac{\partial\boldsymbol{P}}{\partial t} = -\langle\psi(\boldsymbol{r},t)|\nabla_{\boldsymbol{R}}\hat{H}_0(\boldsymbol{r},\boldsymbol{R}(t))|\psi(\boldsymbol{r},t)\rangle, \tag{7}$$

where $\boldsymbol{P}$ is the nuclear momenta on the average PES, $\hat{H}_0(\boldsymbol{r},\boldsymbol{R}(t))$ is the electronic Hamiltonian at the specified nuclear coordinates $\boldsymbol{R}(t)$, and $\psi(\boldsymbol{r},t)$ is the electronic wavefunction at time t. By substituting the adiabatic expansion of the wavefunction into Eq. (7), we can derive the equation for the nuclear motion in the adiabatic representation,

$$\frac{\partial\boldsymbol{P}}{\partial t} = -\sum_i\left(w_i w_i^*\nabla_{\boldsymbol{R}}E_i\right) + \sum_{i,k}\boldsymbol{d}_{ik}\, w_k w_i^*(E_i - E_k). \tag{8}$$

In the following study, we denote the force of the average PES in Eq. (8) as $\boldsymbol{F}_{MF}$, which also uses information from both active and nonactive PESs.

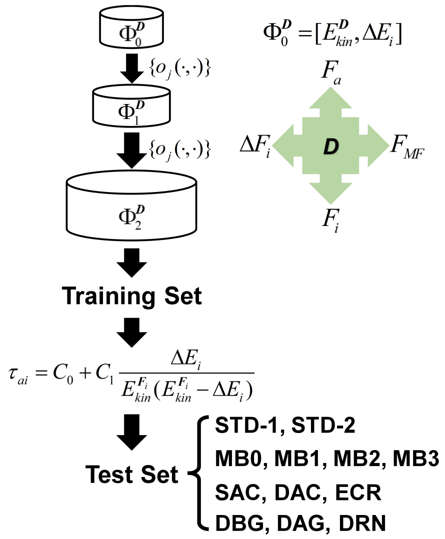

Figure 1. Schematic workflow of the screening processes for decoherence time formulas assisted by machine learning. The initial descriptor space is defined as $\Phi_0^{\boldsymbol{D}} = \left[E^{\boldsymbol{D}}_{kin}, \Delta E_i\right]$, where $\Delta E_i = E_i - E_a$ and $\boldsymbol{D}$ is a chosen force direction which has four different options (i.e., $\boldsymbol{F}_a$, $\boldsymbol{F}_i$, $\Delta\boldsymbol{F}_i$, and $\boldsymbol{F}_{MF}$). Through iterative generation with a series of binary operations $\{o_j(\cdot,\cdot)\}$, we can obtain four different second-order descriptor spaces (i.e., $\Phi_2^{\boldsymbol{F}_a}$, $\Phi_2^{\boldsymbol{F}_i}$, $\Phi_2^{\Delta\boldsymbol{F}_i}$, and $\Phi_2^{\boldsymbol{F}_{MF}}$) with a total number of 1,484 descriptors. After screening with the training set, we obtain the optimal decoherence time formula and benchmark it against a test set with a wide array of one-dimensional and two-dimensional model systems.

As the detailed machine learning algorithms to obtain the optimal decoherence time formula have been described elsewhere [48,49], we here only give a brief introduction and the workflow in **Figure 1**. A large number of candidate descriptors are generated in an iterative manner. Namely, the initial descriptor space is defined as $\Phi_0^{\boldsymbol{D}} = [E^{\boldsymbol{D}}_{kin}, \Delta E_i]$, where $\Delta E_i = E_i - E_a$ and $\boldsymbol{D}$ is a chosen force direction. We then obtain the descriptor space $\Phi_1^{\boldsymbol{D}}$ by applying a series of selected binary operations to $\Phi_0^{\boldsymbol{D}}$, and subsequently generate $\Phi_2^{\boldsymbol{D}}$, which involves applying the same binary operations to all the descriptors in both $\Phi_0^{\boldsymbol{D}}$ and $\Phi_1^{\boldsymbol{D}}$. By design, we obtain four different second-order descriptor spaces, i.e., $\Phi_2^{\boldsymbol{F}_a}$, $\Phi_2^{\boldsymbol{F}_i}$, $\Phi_2^{\Delta\boldsymbol{F}_i}$, and $\Phi_2^{\boldsymbol{F}_{MF}}$, each of which contains 371 descriptors. For each descriptor f, a decoherence time formula is defined as $\tau_{ai} = C_0 + C_1 f$. We adopt 24 one-dimensional and two-dimensional models as the training set and calculate the error function by

$$\epsilon_{train} = \sqrt{\frac{1}{N_{sample}N_{channel}}\sum_{i=1}^{N_{sample}}\sum_{j=1}^{N_{channel}}(P_{ij}^{SH}-P_{ij}^{DVR})^2}. \tag{9}$$

Here, the number of channels $N_{channel}$ is 8, while the number of samples N_{sample} is 24. P_{ij}^{SH} and P_{ij}^{DVR} are populations of the jth channel in the ith sample at the final snapshot calculated by surface hopping (SH) and the discrete variable representation (DVR) [52], respectively. Note that the decoherence time here is a physically motivated quantity introduced to enhance the accuracy of mixed quantum-classical dynamics simulations. It is not a priori known along trajectories, and an analytical gradient of the error function cannot be derived. Thus, we here continue to employ the discrete space optimization to determine the parameters [48].

In **Figure 2**, we show the error distribution of surface hopping simulations with the decoherence time formulas defined based on all the descriptors in the four descriptor spaces of $\Phi_2^{\boldsymbol{F}_a}$, $\Phi_2^{\boldsymbol{F}_i}$, $\Phi_2^{\Delta\boldsymbol{F}_i}$, and $\Phi_2^{\boldsymbol{F}_{MF}}$. It is apparent that the overall behavior of the descriptors looks similar across the four descriptor spaces, with the majority of descriptor errors concentrated around 0.019, while the minimum error is approximately 0.013. Encouragingly, Eq. (3) consistently stands out in the four different descriptor spaces, exhibiting either the smallest or the second smallest error in the corresponding set of descriptors. The relevant parameters in the decoherence time formulas of Eq. (3) along with the associated training errors are detailed in **Table 1**. It is important to note that Eq. (3) with $E_{kin}^{\boldsymbol{F}_i}$ not only gives the smallest error within the $\Phi_2^{\boldsymbol{F}_i}$ space but also achieves the lowest error among all the four descriptor spaces. Thereby, the optimal decoherence time formula obtained in the training set is

$$\tau_{ai} = C_0 + C_1\frac{\Delta E_i}{E_{kin}^{\boldsymbol{F}_i}(E_{kin}^{\boldsymbol{F}_i}-\Delta E_i)}, \tag{10}$$

where C_0 = 4×10⁶ and C_1 = 1000. Although both ref. 49 and the present study yield the optimal decoherence time formula in the form of Eq. (3), it is important to clarify that this is obtained independently. Namely, Eq. (3) emerges only after a careful selection from the descriptor spaces (i.e., $\Phi_2^{\boldsymbol{F}_a}$, $\Phi_2^{\boldsymbol{F}_i}$, $\Phi_2^{\Delta\boldsymbol{F}_i}$, and $\Phi_2^{\boldsymbol{F}_{MF}}$) in this study, thus also confirming the general applicability of this expression.

To quantitatively evaluate the performance of decoherence time formulas based on different force-projected kinetic energies in the form of Eq. (3), we calculate the average population error in a large number of test systems for the initial momentum k by

$$\epsilon_{test}(k) = \sqrt{\frac{1}{N_{init}N_{channel}}\sum_{i=1}^{N_{init}}\sum_{j=1}^{N_{channel}}(P_{ij}^{SH}-P_{ij}^{DVR})^2}, \tag{11}$$

Table 1. Relevant parameters in the decoherence time formula of Eq. (3) and associated errors for surface hopping simulations obtained using different choices of $\boldsymbol{D}$ in the same training set.

$\boldsymbol{D}$	C_0	C_1	Error
$\boldsymbol{F}_i$	4×10⁶	1000	0.0123
$\boldsymbol{F}_a$	1×10⁶	125	0.0136
$\Delta\boldsymbol{F}_i$	4×10⁴	100	0.0144
$\boldsymbol{F}_{MF}$	8×10⁶	62.5	0.0153

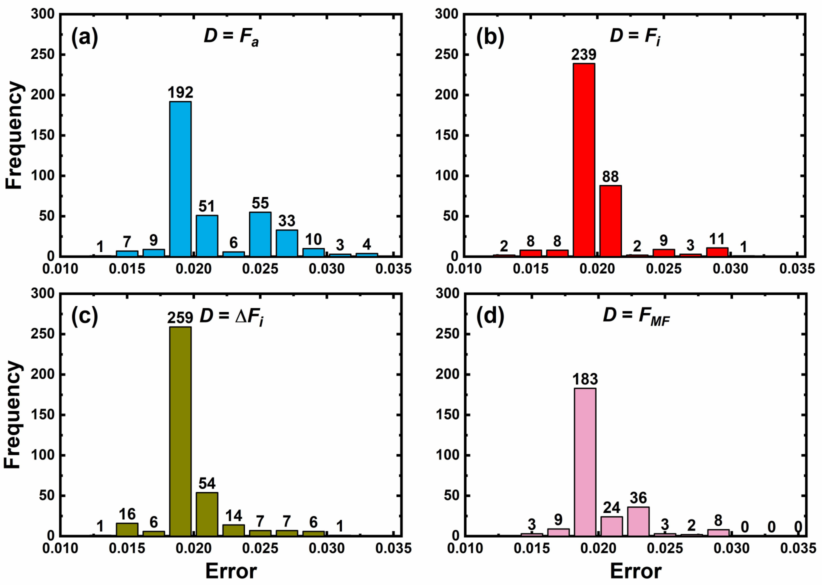

Figure 2. Error distribution of surface hopping simulations using the decoherence time formulas defined based on descriptors from (a) $\Phi_2^{\boldsymbol{F}_a}$, (b) $\Phi_2^{\boldsymbol{F}_i}$, (c) $\Phi_2^{\Delta\boldsymbol{F}_i}$, and (d) $\Phi_2^{\boldsymbol{F}_{MF}}$ spaces in the training set. The errors associated with the descriptors which are not shown in (d) are all above 0.07.

where N_{init} denotes the number of initial conditions for each test system, and $N_{channel}$ represents the number of final channels, which is determined by the number of energy levels and the system dimensionality. We first examine the performance of Eq. (3) with $E_{kin}^{\boldsymbol{F}_a}$, $E_{kin}^{\boldsymbol{F}_i}$, $E_{kin}^{\Delta\boldsymbol{F}_i}$, and $E_{kin}^{\boldsymbol{F}_{MF}}$ in two two-dimensional systems, namely the STD-1 and STD-2 models [50,53]. In the STD-1 model [53], the Hamiltonian reads

$$H_{11}(x,y) = -A_1 \tanh(B_1 x), \tag{12}$$

$$H_{22}(x,y) = A_2 \tanh[B_2(x-1) + C_2\cos(D_2 y + \pi/2)] \\ +3A_2/4, \tag{13}$$

$$H_{12}(x,y) = H_{21}(x,y) = A_3 \exp(-B_3 x^2), \tag{14}$$

where A_1 = 0.05, B_1 = 0.6, A_2 = 0.2, B_2 = 0.6, C_2 = 2.0, D_2 = 0.3, A_3 = 0.015, and B_3 = 0.3. The initial wave packet is placed on either the lower or the upper surface at coordinates (x_0, y_0), with x_0 = -4.0 and y_0 selected from {-2.0, -1.0, 0, 1.0, 2.0, 3.0, 4.0, 5.0}. The direction of the initial momentum is specified by an angle θ_0 relative to the x-axis, which takes values of 0°, 15°, 30°, or 45°. For cases where the initial wave packet is located on the lower (or upper) surface, the momentum ranges from 16 to 28 (or 8 to 20), respectively.

For the STD-1 model, the error function in Eq. (11) with N_{init} = 32 and $N_{channel}$ = 8 is used to evaluate the performance of surface hopping simulations. As shown in **Figure 3a**, the standard FSSH method has large errors within 0.03-0.06 in the entire momentum range when the initial wave packet is on the upper surface. After introducing quantum decoherence correction via Eq. (3) with $E_{kin}^{\boldsymbol{F}_{MF}}$, the errors are significantly reduced to below 0.03. In particular, when using Eq. (3) with $E_{kin}^{\boldsymbol{F}_i}$, the errors are uniformly smaller than 0.02. In comparison, Eq. (3) performs poorly with $E_{kin}^{\boldsymbol{F}_a}$ or $E_{kin}^{\Delta\boldsymbol{F}_i}$, which even show larger errors in the high-momentum region than FSSH which does not have decoherence correction. Instead, when the initial wave packet is located on the lower surface, the error of FSSH generally falls between 0.025 and 0.03 (see **Figure 3c**). After introducing decoherence correction using Eq. (3) with $E_{kin}^{\boldsymbol{F}_{MF}}$, the error stabilizes at approximately 0.015. Overall, except for Eq. (3) with $E_{kin}^{\Delta\boldsymbol{F}_i}$, all other three decoherence time formulas consistently yield lower errors than FSSH across the entire momentum range.

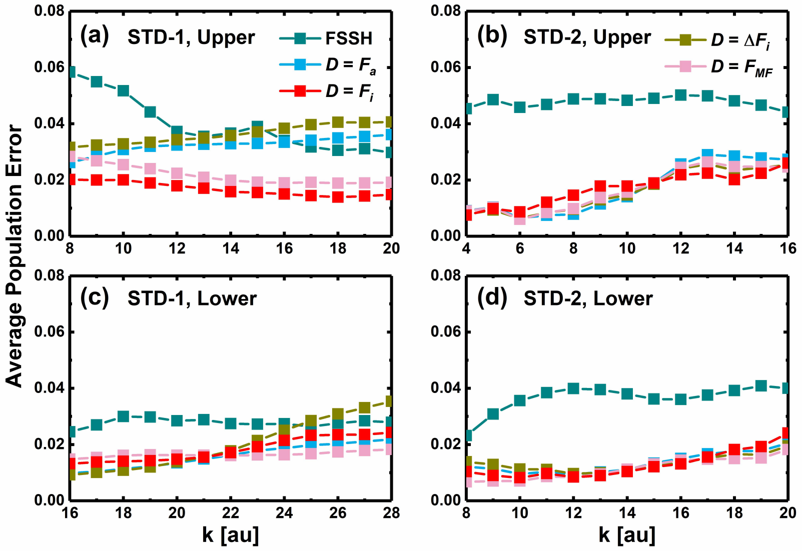

Figure 3. Average population errors of surface hopping with different decoherence time formulas for the STD-1 model initialized from the (a) upper and (c) lower surfaces, and the STD-2 model initialized from the (b) upper and (d) lower surfaces. The errors of FSSH are shown by dark cyan solid squares. For comparison, the errors of FSSH using different decoherence time formulas of Eq. (3) with $E_{kin}^{\boldsymbol{F}_a}$, $E_{kin}^{\boldsymbol{F}_i}$, $E_{kin}^{\Delta\boldsymbol{F}_i}$, and $E_{kin}^{\boldsymbol{F}_{MF}}$ are represented by blue, red, ginger yellow, and pink solid squares, respectively.

We further consider the STD-2 model [50]. The diabatic Hamiltonian is expressed as

$$H_{11}(x,y) = -E_0, \tag{15}$$

$$H_{22}(x,y) = -A\exp\{-B[0.75(x+y)^2 \\ +0.25(x-y)^2]\}, \tag{16}$$

$$H_{12}(x,y) = H_{21}(x,y) = C\exp\{-D[0.25(x+y)^2 \\ +0.75(x-y)^2]\}, \tag{17}$$

where A = 0.15, B = 0.14, C = 0.015, D = 0.06, and E_0 = 0.05. The error function of Eq. (11) with N_{init} = 18 and $N_{channel}$ = 8 is utilized. It is apparent that the errors of surface hopping are significantly reduced compared to those of FSSH after incorporating the decoherence correction of Eq. (3), particularly when the initial wave packet is located on the upper surface (see **Figure 3b**). Unlike the results obtained in the STD-1 model, Eq. (3) exhibits consistently high performance when paired with $E_{kin}^{\boldsymbol{F}_a}$, $E_{kin}^{\boldsymbol{F}_i}$, $E_{kin}^{\Delta\boldsymbol{F}_i}$, or $E_{kin}^{\boldsymbol{F}_{MF}}$. Overall, Eq. (3) with $E_{kin}^{\boldsymbol{F}_i}$ or $E_{kin}^{\boldsymbol{F}_{MF}}$ shows more consistent and relatively higher performance in the two two-dimensional test systems (i.e., STD-1 and STD-2 models). Note that we have considered 832 and 468 initial conditions for STD-1 and STD-2 models, respectively. As each initial condition results in 8 channel populations here, we have considered 10,400 channel populations in total for the two representative two-dimensional models, which form a rich set of data. With the training data restricted to the final channel populations, accurate description of time-dependent populations would further validate the obtained formula. Preliminary results indicate that incorporation of Eq. (10) into surface hopping also yields substantial improvements in the time evolution.

To further assess the robustness of surface hopping with decoherence corrections, we expand the investigation of Eq. (3) with $E_{kin}^{\boldsymbol{F}_i}$ and $E_{kin}^{\boldsymbol{F}_{MF}}$ to one-dimensional multi-level systems, which provide a much larger number of test systems. In detail, we consider a series of benchmark model bases, including the two-level model base MB0, the three-level model base MB1, the four-level model base MB2, and a special three-level model base MB3 which contains models with exponential and Morse repulsive potentials [41,54]. It is important to note that the training set above contains only 4 one-dimensional two-level samples. Thereby, these model bases render a comprehensive evaluation of the applicability of decoherence time formulas in complex multi-level scenarios.

In the two-level model base MB0 [41], five distinct function forms are considered for the diagonal elements of the diabatic Hamiltonian,

$$H_{11}^{[1]} = E_1, \tag{18}$$

$$H_{22}^{[1]} = E_2, \tag{19}$$

$$H_{11}^{[2]} = \begin{cases} E_2 - A_1[1 - \exp(B_1 x)], & x < 0 \\ E_2 + A_1[1 - \exp(-B_1 x)], & x > 0 \end{cases} \tag{20}$$

$$H_{22}^{[2]} = \begin{cases} E_3 - A_1[1 - \exp(B_1 x)], & x < 0 \\ E_3 + A_1[1 - \exp(-B_1 x)], & x > 0 \end{cases} \tag{21}$$

$$H_{11}^{[3]} = \begin{cases} -E_2 + A_1[1 - \exp(B_1 x)], & x < 0 \\ -E_2 - A_1[1 - \exp(-B_1 x)], & x > 0 \end{cases} \tag{22}$$

$$H_{22}^{[3]} = \begin{cases} E_1 + A_1[1 - \exp(B_1 x)], & x < 0 \\ E_1 - A_1[1 - \exp(-B_1 x)], & x > 0 \end{cases} \tag{23}$$

$$H_{11}^{[4]} = E_1 + A_2 \exp(-B_2 x^2), \tag{24}$$

$$H_{22}^{[4]} = E_2 + A_2 \exp(-B_2 x^2), \tag{25}$$

$$H_{11}^{[5]} = E_1 - A_2 \exp(-B_2 x^2), \tag{26}$$

$$H_{22}^{[5]} = E_2 - A_2 \exp(-B_2 x^2), \tag{27}$$

where $A_1 = 0.01$, $B_1 = 1.6$, $A_2 = 0.02$, $B_2 = 0.28$, $E_1 = 0$, $E_2 = 0.01$, and $E_3 = 0.02$. For the off-diagonal elements of the Hamiltonian, we adopt the Gaussian-type function,

$$H_{12} = H_{21} = S \exp(-W x^2). \tag{28}$$

Here, S and W respectively represent the strength and spatial width of the diabatic coupling. In MB0, S takes four different values (i.e., 0.0025, 0.005, 0.02, and 0.04), corresponding to gradually enhanced diabatic coupling strengths. And W takes two values (i.e., 0.4 and 1.5), representing broad and narrow spatial distributions of the diabatic coupling, respectively.

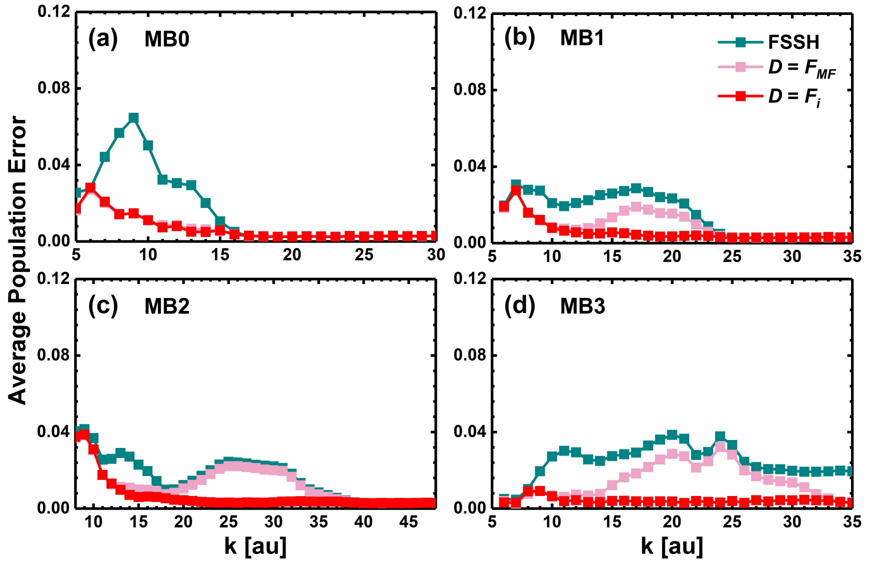

Figure 4. Average population errors of FSSH and FSSH with Eq. (3) based on different forces for (a) the two-level model base MB0 which comprises 200 models with 26 distinct initial momenta, (b) the three-level model base MB1 consisting of 750 models with 30 different initial momenta, (c) the four-level model base MB2 containing 625 models with 41 different initial momenta, and (d) the model base MB3 which includes 50 models with strong repulsive potentials and 30 different initial momenta. The errors of FSSH and FSSH using Eq. (3) with $E_{kin}^{\boldsymbol{F}_{MF}}$ and $E_{kin}^{\boldsymbol{F}_i}$ are shown by dark cyan, pink and red solid lines, respectively.

Based on the 25 distinct diagonal terms and 8 combinations of off-diagonal terms, there are 200 different one-dimensional two-level models in MB0 [41]. In **Figure 4a**, we show the momentum-dependent population errors of MB0, which are calculated with $N_{init} = 200$ and $N_{channel} = 4$. For $k > 16$, the errors of all the three methods are below 0.003 due to the incorporation of phase correction in surface hopping. In the absence of decoherence correction, however, significant errors are observed for small k. In particular, when k = 9, the FSSH error is about 0.065. In contrast, after applying the decoherence correction in Eq. (3) with $E_{kin}^{\boldsymbol{F}_i}$ or $E_{kin}^{\boldsymbol{F}_{MF}}$, the average population errors drop to less than 0.02 for $k > 6$ and monotonically decrease as k increases. Overall, the performance of surface hopping based on both $E_{kin}^{\boldsymbol{F}_i}$ and $E_{kin}^{\boldsymbol{F}_{MF}}$ is similar in MB0.

It is generally expected that an increase in the number of energy levels enhances the complexity of nonadiabatic dynamics. Thereby, we further make a systematic study in three-level and four-level systems. The model base MB1 consists of a collection of scattering models featuring three energy levels and one classical degree of freedom [54]. The diagonal elements of the Hamiltonian take five different forms, which are

$$H_{11}^{[1]} = E_1 + C_1, \tag{29}$$

$$H_{22}^{[1]} = E_2 + C_2, \tag{30}$$

$$H_{33}^{[1]} = E_3 + C_3, \tag{31}$$

$$H_{11}^{[2]} = \begin{cases} E_2 - A_1[1 - \exp(B_1 x)] + C_1, & x < 0 \\ E_2 + A_1[1 - \exp(-B_1 x)] + C_1, & x > 0 \end{cases} \tag{32}$$

$$H_{22}^{[2]} = \begin{cases} E_3 - A_1[1 - \exp(B_1 x)] + C_2, & x < 0 \\ E_3 + A_1[1 - \exp(-B_1 x)] + C_2, & x > 0 \end{cases} \tag{33}$$

$$H_{33}^{[2]} = \begin{cases} E_4 - A_1[1 - \exp(B_1 x)] + C_3, & x < 0 \\ E_4 + A_1[1 - \exp(-B_1 x)] + C_3, & x > 0 \end{cases} \tag{34}$$

$$H_{11}^{[3]} = \begin{cases} -E_2 + A_1[1 - \exp(B_1 x)] + C_1, & x < 0 \\ -E_2 - A_1[1 - \exp(-B_1 x)] + C_1, & x > 0 \end{cases} \tag{35}$$

$$H_{22}^{[3]} = \begin{cases} E_1 + A_1[1 - \exp(B_1 x)] + C_2, & x < 0 \\ E_1 - A_1[1 - \exp(-B_1 x)] + C_2, & x > 0 \end{cases} \tag{36}$$

$$H_{33}^{[3]} = \begin{cases} E_2 + A_1[1 - \exp(B_1 x)] + C_3, & x < 0 \\ E_2 - A_1[1 - \exp(-B_1 x)] + C_3, & x > 0 \end{cases} \tag{37}$$

$$H_{11}^{[4]} = E_1 + A_2 \exp(-B_2 x^2) + C_1, \tag{38}$$

$$H_{22}^{[4]} = E_2 + A_2 \exp(-B_2 x^2) + C_2, \tag{39}$$

$$H_{33}^{[4]} = E_3 + A_2 \exp(-B_2 x^2) + C_3, \tag{40}$$

$$H_{11}^{[5]} = E_1 - A_2 \exp(-B_2 x^2) + C_1, \tag{41}$$

$$H_{22}^{[5]} = E_2 - A_2 \exp(-B_2 x^2) + C_2, \tag{42}$$

$$H_{33}^{[5]} = E_3 - A_2 \exp(-B_2 x^2) + C_3, \tag{43}$$

where E_1 = 0, E_2 = 0.01, E_3 = 0.02, E_4 = 0.03, C_1 = 0, C_2 = 0.005, C_3 = 0.01, A_1 = 0.01, A_2 = 0.02, B_1 = 1.6, and B_2 = 0.28. In addition, three types of Gaussian diabatic couplings are considered to characterize the off-diagonal elements of the Hamiltonian, which are expressed as

$$H_{12} = H_{21} = S_1 \exp(-W_1 x^2), \tag{44}$$

$$H_{23} = H_{32} = S_2 \exp(-W_2 x^2), \tag{45}$$

$$H_{13} = H_{31} = S_3 \exp(-W_3 x^2), \tag{46}$$

We consider two sets of coupling strengths, i.e., (S_1 = 0.04, S_2 = 0.03, S_3 = 0.005) and (S_1 = 0.10, S_2 = 0.05, S_3 = 0.01), along with three sets of coupling widths, i.e., W_1 = W_2 = W_3 = 0.3, 0.6, and 1.5. As there exist 125 combinations of diabatic potential surfaces and 6 sets of diabatic couplings, MB1 contains a total number of 750 one-dimensional three-level models.

We also consider a four-level model base MB2 [54]. While the first three diagonal elements of the Hamiltonian are the same as those in Eqs. (29)-(43), the fourth diagonal element is chosen from the following five expressions,

$$H_{44}^{[1]} = E_4 + C_4, \tag{47}$$

$$H_{44}^{[2]} = \begin{cases} E_5 - A_1[1 - \exp(B_1 x)] + C_4, & x < 0 \\ E_5 + A_1[1 - \exp(-B_1 x)] + C_4, & x > 0 \end{cases} \tag{48}$$

$$H_{44}^{[3]} = \begin{cases} E_3 + A_1[1 - \exp(B_1 x)] + C_4, & x < 0 \\ E_3 - A_1[1 - \exp(-B_1 x)] + C_4, & x > 0 \end{cases} \tag{49}$$

$$H_{44}^{[4]} = E_4 + A_2 \exp(-B_2 x^2) + C_4, \tag{50}$$

$$H_{44}^{[5]} = E_4 - A_2 \exp(-B_2 x^2) + C_4, \tag{51}$$

where E_3 = 0.02, E_4 = 0.03, E_5 = 0.04, C_4 = 0.025, A_1 = 0.01, A_2 = 0.02, B_1 = 1.6, and B_2 = 0.28. The six off-diagonal terms are defined as

$$H_{12} = H_{21} = S_1 \exp(-W_1 x^2), \tag{52}$$

$$H_{23} = H_{32} = S_2 \exp(-W_2 x^2), \tag{53}$$

$$H_{34} = H_{43} = S_3 \exp(-W_3 x^2), \tag{54}$$

$$H_{13} = H_{31} = S_4 \exp(-W_4 x^2), \tag{55}$$

$$H_{24} = H_{42} = S_5 \exp(-W_5 x^2), \tag{56}$$

$$H_{14} = H_{41} = S_6 \exp(-W_6 x^2), \tag{57}$$

where $S_1 = S_2 = S_3 = 0.16$, $S_4 = S_5 = 0.06$, $S_6 = 0.01$, and $W_1 = W_2 = W_3 = W_4 = W_5 = W_6 = 1.5$, reflecting strong and narrow couplings between energetically adjacent states. Since each diagonal term of the Hamiltonian has five options, MB2 contains 625 models in total.

In **Figure 4b**, we show the average population errors of MB1 with N_{init} = 750 and $N_{channel}$ = 6. It is apparent that the most significant difference among the three methods lies in the region with k < 25. For instance, the FSSH method exhibits an error of approximately 0.03 for k = 17. In comparison, this error is reduced to about 0.02 by incorporating decoherence by Eq. (3) with $E_{kin}^{\boldsymbol{F}_{MF}}$. Using Eq. (3) with $E_{kin}^{\boldsymbol{F}_i}$ leads to a more significant reduction in error, with a value down to 0.004. In these three-level systems, the differences between $E_{kin}^{\boldsymbol{F}_{MF}}$ and $E_{kin}^{\boldsymbol{F}_i}$ begin to surface, while Eq. (3) with $E_{kin}^{\boldsymbol{F}_i}$ continues to show high performance.

As shown in **Figure 4c**, we further explore whether Eq. (3) with $E_{kin}^{\boldsymbol{F}_i}$ could have stable and high performance in the four-level model base MB2. Similar to the performance in MB1, FSSH shows unsatisfactory average population errors calculated with N_{init} = 625 and $N_{channel}$ = 8. In particular, the behavior of Eq. (3) with $E_{kin}^{\boldsymbol{F}_{MF}}$ becomes closer to that of FSSH in the intermediate momentum region as the number of energy levels increases. This is primarily due to the fact that, in the investigated models, higher energy levels are generally associated with higher potential barriers. For the intermediate k, the kinetic energy is not large enough to surpass the potential barrier and stronger decoherence effects are present. The utilization of $E_{kin}^{\boldsymbol{F}_{MF}}$ fails to capture such strong decoherence effect adequately.

Except the three model bases studied above, when atoms, molecules, and metal surfaces collide, the corresponding PESs show significant repulsive behavior. Thus, we also study the MB3 model base [54], which adopts the exponential and Morse potentials to describe the third diabatic PES,

$$H_{33}^{[6]} = A_6^{-x}/B_6 + E_4, \tag{58}$$

$$H_{33}^{[7]} = -A_7 + A_7[1 - \exp(B_7 x)]^2 + E_6. \tag{59}$$

Here, A_6 = 0.8, A_7 = 0.08, B_6 = 15, B_7 = 0.13, E_4 = 0.03, and E_6 = 0.1. While the first two diagonal elements of the Hamiltonian still follow the forms and parameters of MB1, the off-diagonal terms of the Hamiltonian adhere to the form in MB1 but have different parameters, namely, S_1 = 0.2, S_2 = 0.1, S_3 = 0.05, and $W_1 = W_2 = W_3$ = 0.6. In these cases, the errors are calculated with N_{init} = 50 and $N_{channel}$ = 6. In significant contrast to the three model bases above, FSSH exhibits considerable errors even in the high k region (see **Figure 4d**). In fact, as infinite potential energy barriers are present in all these systems, the decoherence correction dominates the performance across all k regions, rather than being limited to the low and intermediate k. The introduction of decoherence correction (Eq. (3) with $E_{kin}^{\boldsymbol{F}_{MF}}$) achieves slightly better performance than FSSH. Encouragingly, Eq. (3) with $E_{kin}^{\boldsymbol{F}_i}$ still consistently shows exceptional performance with the average population errors below 0.01 in all cases.

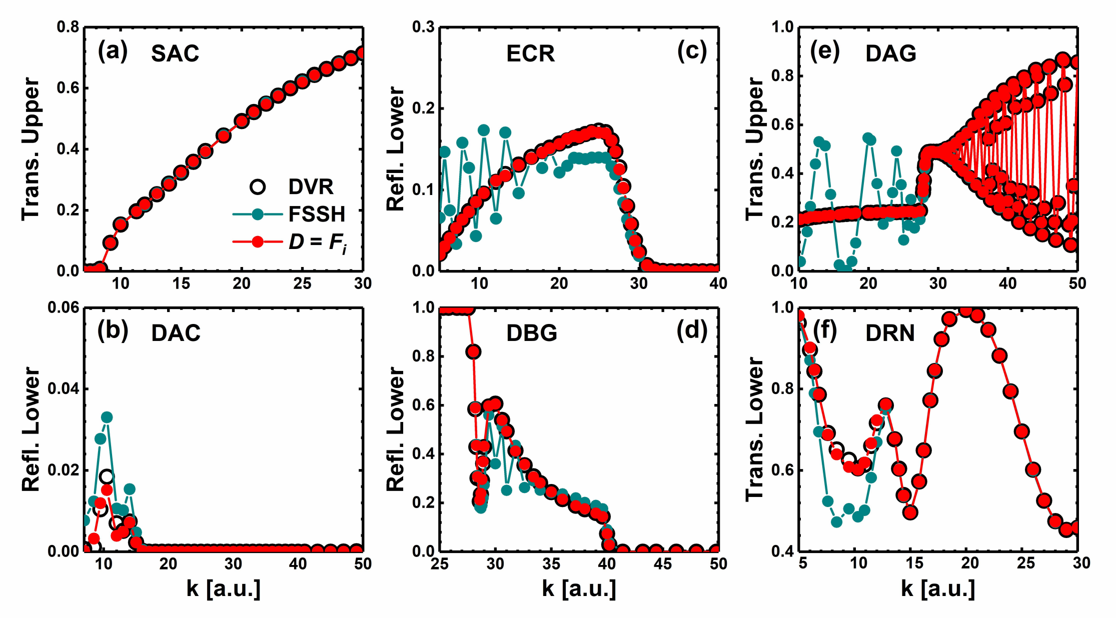

Figure 5. (a) Transmission probability on the upper surface for the SAC model, (b) reflection probability on the lower surface for the DAC model, (c) reflection probability on the lower surface for the ECR model, (d) reflection probability on the lower surface for the DBG model, (e) transmission probability on the upper surface for the DAG model, and (f) transmission probability on the lower surface for the DRN model. The black open circles are the exact quantum solutions by DVR. The results of FSSH and FSSH using decoherence correction in Eq. (3) with $E_{kin}^{\boldsymbol{F}_i}$ are shown as dark cyan and red solid circles, respectively.

For all the four model bases investigated above, it is evident that, aside from the few small k points, Eq. (3) with $E_{kin}^{\boldsymbol{F}_i}$ (i.e., Eq. (10)) results in negligible errors below 0.01 in most calculations. Since 1990, the three Tully models, i.e., the simple avoided crossing (SAC), the dual avoided crossing (DAC), and the extended coupling with reflection (ECR) models, have served as standard benchmark systems for new nonadiabatic dynamics simulation methods [34,55]. In addition, three more challenging models have been introduced, namely the dumbbell geometry (DBG), the double arch geometry (DAG), and the dual Rosen-Zener-Demkov non-crossing (DRN) models [47,56]. Thereby, we here also adopt these six models to thoroughly assess the performance of Eq. (3) with $E_{kin}^{\boldsymbol{F}_i}$. Since these models are well known, we present only a single representative channel per model to ensure the clarity of results. In **Figure 5a** and **Figure 5b**, we show the transmission populations on the upper surface for the SAC model and the reflection populations on the lower surface for the DAC model. The FSSH results are satisfactory and in line with the exact quantum solutions. After applying the decoherence correction using Eq. (3) with $E_{kin}^{\boldsymbol{F}_i}$, the results are almost identical to those of FSSH in the SAC model, but provide a much more accurate description of the DAC model.

In **Figure 5c** and **Figure 5d**, we show the reflection populations on the lower surfaces for the ECR and DBG models. The standard FSSH with phase correction generally gives oscillating reflection probabilities for relatively small k. Encouragingly, after decoherence correction using Eq. (3) with $E_{kin}^{\boldsymbol{F}_i}$, these oscillations are completely eliminated and the results agree very well with the exact quantum solutions. In **Figure 5e** and **Figure 5f**, we show the transmission populations on the upper surface for the DAG model and those on the lower surface for the DRN model. These two models are more complex, as nonadiabatic dynamics simulations require a finely tuned balance between coherence and decoherence. In the DAG model, FSSH exhibits oscillatory results in the entire k range (see **Figure 5e**), indicating that the dynamics is overcoherent. In comparison, Eq. (3) with $E_{kin}^{\boldsymbol{F}_i}$ gives smooth results for small k and oscillatory results for large k, which are fully consistent with the exact solutions. FSSH also fails to describe the transmission in the small k region of the DRN model (see **Figure 5f**), while Eq. (3) with $E_{kin}^{\boldsymbol{F}_i}$ consistently yields results that closely reproduce the exact solutions. Note that in Eq. (10), C_0 is a relatively large value. This is reasonable because the decoherence strength should be negligible when ΔE_i is very small. We also investigated the formula with only C_0 in the three Tully models, which yields similar results with the traditional FSSH.

To summarize, we have utilized machine learning to obtain optimal decoherence time formulas based on the force-projected kinetic energy. Four different types of forces have been considered as feature inputs in the decoherence time formulas, and the form of Eq. (3) has been found to consistently stand out. Through a systematic benchmark, we have identified that Eq. (3) with $E_{kin}^{\boldsymbol{F}_i}$ (i.e., Eq. (10)) shows the highest performance across all the investigated scattering systems, including two-dimensional two-level models (i.e, STD-1 and STD-2), one-dimensional multi-level model bases (i.e., MB0, MB1, MB2, and MB3), as well as six standard one-dimensional models (i.e., SAC, DAC, ECR, DBG, DAG, and DRN). However, high-dimensional scattering models and more realistic systems are important for assessing the generalizability of decoherence time formulas, which deserves systematic studies in the future. Note that as a preliminary validation of Eq. (10) in a more realistic setting, a photodissociation model can be considered [37,57]. While the obtained time-dependent populations agree well with the exact quantum solutions, the traditional FSSH yields similiarly accurate results in this model, indicating the applicability of Eq. (10) in the weak decoherence regime. In the present study, we have extended the framework of machine learning decoherence time from one-dimensional scattering models to identify the optimal decoherence time formula applicable to both one- and two-dimensional systems, thereby further supporting the generality of studying complex decoherence effects in nonadiabatic dynamics based on machine learning.

Finally, we note that when considering the utilization of force direction for decoherence correction, the active state is typically the first option that comes to our mind. However, the systematic study here has suggested that the force associated with the corresponding nonactive state is actually more suitable. As the force F_a primarily determines the nuclear motion on the active PES, projection of the kinetic energy along F_a tends to overemphasize the dynamics on the active PES and does not capture the separation of wave packet components on different surfaces, which is associated with strong decoherence [37]. More insights can be gained from the wave packet reflection criterion introduced in the branching corrected surface hopping (BCSH) method.[41] In this approach, if the dot products $\boldsymbol{F}_i(t) \cdot \boldsymbol{P}_i(t)$ and $\boldsymbol{F}_i(t) \cdot \boldsymbol{P}_i(t + \Delta t)$ have opposite signs, a wave packet reflection event is considered to occur on the ith PES during the time interval Δt. Based on the assumption of parallel momenta, we may have $\boldsymbol{P}_i = \eta \boldsymbol{P}_a$, where $\boldsymbol{P}_a$ and $\boldsymbol{P}_i$ are nuclear momenta on the active and nonactive PESs. This implies that the identification of wave packet reflection on nonactive PESs requires the information about the velocity on the active PES as well as the force on the nonactive PES. In this regard, it is natural that the calculation of decoherence time requires the utilization of the kinetic energy component that is associated with the direction of force acting on the nonactive PES (i.e., $E_{kin}^{\boldsymbol{F}_i}$). Furthermore, decoherence correction is also essential in condensed-phase systems. Simulations with decoherence correction are not necessarily always more accurate than uncorrected ones [58]. This highlights the central challenge of quantum decoherence correction: it should be applied only when appropriate [37,41]. In this regard, identifying a universal function form that can be used to treat nonadiabatic dynamics in a broadly applicable manner is conceptually analogous to the design of general exchange-correlation functional in density functional theory. More efforts should be devoted to achieving this goal. In terms of the computational efficiency, the proposed decoherence correction based on force-projected kinetic energies is similar to that of BCSH[41] but is higher than that of the purely energy-based decoherence time formula.[46] However, considering that higher accuracy may be achieved, it is still useful in many applications. In particular, when employing machine learning Hamiltonians [19,59,60], the corresponding forces can be analytically calculated, which keeps the additional computational overhead at a reasonable level even for large complex realistic systems.

Acknowledgments

We acknowledge support from the National Natural Science Foundation of China (Grant No. 22273082), Zhejiang Provincial Natural Science Foundation of China (Grant No. LZ25B030001), the Fundamental Research Funds for the Zhejiang Provincial Universities (Grant No. 226-2025-00260), the Open Project Fund of National Facility for Translational Medicine (Shanghai) (Grant No. TMSK-2024-109), and the High-Performance Computing Center in Department of Chemistry, Zhejiang University.

References

[1] Granucci G., Persico M. and Toniolo A., Direct semiclassical simulation of photochemical processes with semiempirical wave functions. *J. Chem. Phys.*, **114** (2001), 10608–10615.

[2] Persico M., Granucci G., Inglese S., Laino T. and Toniolo A., Semiclassical simulation of photochemical reactions in

condensed phase. *J. Mol. Struct.: Theochem,* **621** (2003), 119–126.

[3] Cusati T., Granucci G. and Persico M., Photodynamics and time-resolved fluorescence of azobenzene in solution: a mixed quantum-classical simulation. *J. Am. Chem. Soc.,* **133** (2011), 5109–5123.

[4] Aziz S.G., Alyoubi A.O., Elroby S.A. and Hilal R.H., Photochemical dissociation of HOBr: a nonadiabatic dynamics study. *J. Photochem. Photobiol. A: Chem.,* **324** (2016), 8–13.

[5] Gao L.-H., Xie B.-B. and Fang W.-H., Theories and applications of mixed quantum-classical non-adiabatic dynamics. *Chin. J. Chem. Phys.,* **31** (2018), 12–26.

[6] Tang D., Shen L. and Fang W.-H., Evaluation of mixed quantum-classical molecular dynamics on cis-azobenzene photoisomerization. *Phys. Chem. Chem. Phys.,* **23** (2021), 13951–13964.

[7] Zhu C., Analytical switching algorithms for global trajectory surface hopping molecular dynamics simulation. *J. Chem. Theory Comput.,* **21** (2025), 7729–7742.

[8] Tiwari V., Peters W.K. and Jonas D.M., Electronic resonance with anticorrelated pigment vibrations drives photosynthetic energy transfer outside the adiabatic framework. *Proc. Natl. Acad. Sci. U.S.A.,* **110** (2013), 1203–1208.

[9] Tao G. and Shen N., Mapping state space to quasiclassical trajectory dynamics in coherence-controlled nonadiabatic simulations for condensed phase problems. *J. Phys. Chem. A,* **121** (2017), 1734–1747.

[10] Mausenberger S., Müller C., Tkatchenko A., Marquetand P., González L. and Westermayr J., SPaiNN: equivariant message passing for excited-state nonadiabatic molecular dynamics. *Chem. Sci.,* **15** (2024), 15880–15890.

[11] Lorenzoni N., Lacroix T., Lim J., Tamascelli D., Huelga S.F. and Plenio M.B., Full microscopic simulations uncover persistent quantum effects in primary photosynthesis. *Sci. Adv.,* **11** (2025), eady6751.

[12] Kambhampati P., Hot exciton relaxation dynamics in semiconductor quantum dots: radiationless transitions on the nanoscale. *J. Phys. Chem. C,* **115** (2011), 22089–22109.

[13] Menke S.M. and Holmes R.J., Exciton diffusion in organic photovoltaic cells. *Energy Environ. Sci.,* **7** (2014), 499–512.

[14] Qiao L., Fang W.-H., Long R. and Prezhdo O.V., Photoinduced dynamics of charge carriers in metal halide perovskites from an atomistic perspective. *J. Phys. Chem. Lett.,* **11** (2020), 7066–7082.

[15] Li W., She Y., Vasenko A.S. and Prezhdo O.V., Ab initio nonadiabatic molecular dynamics of charge carriers in metal halide perovskites. *Nanoscale,* **13** (2021), 10239–10265.

[16] Deng Y., Peng F., Lu Y., Zhu X., Jin W., Qiu J., Dong J., Hao Y., Di D., Gao Y., Sun T., Zhang M., Liu F., Wang L., Ying L., Huang F. and Jin Y., Solution-processed green and blue quantum-dot light-emitting diodes with eliminated charge leakage. *Nat. Photonics,* **16** (2022), 505–511.

[17] Lu Y., Dong J. and Wang L., Importance sampling for equilibrium properties in non-adiabatic systems: application to anomalous interfacial charge transfer. *J. Phys. Chem. C,* **127** (2023), 10861–10870.

[18] Wang Z., Dong J. and Wang L., Large-scale surface hopping simulation of charge transport in hexagonal molecular crystals: role of electronic coupling signs. *J. Phys.: Condens. Matter,* **35** (2023), 345401.

[19] Cao B., Dong J., Wang Z. and Wang L., Large-scale non-adiabatic dynamics simulation based on machine learning Hamiltonian and force field: the case of charge transport in monolayer MoS_2. *J. Phys. Chem. Lett.,* **16** (2025), 4907–4920.

[20] Parandekar P.V. and Tully J.C., Mixed quantum-classical equilibrium. *J. Chem. Phys.,* **122** (2005), 094102.

[21] Wang L., Akimov A. and Prezhdo O.V., Recent progress in surface hopping: 2011–2015. *J. Phys. Chem. Lett.,* **7** (2016), 2100–2112.

[22] Crespo-Otero R. and Barbatti M., Recent advances and perspectives on nonadiabatic mixed quantum-classical dynamics. *Chem. Rev.,* **118** (2018), 7026–7068.

[23] Wang L., Qiu J., Bai X. and Xu J., Surface hopping methods for nonadiabatic dynamics in extended systems. *WIREs Comput. Mol. Sci.,* **10** (2020), e1435.

[24] Tapavicza E., Tavernelli I. and Rothlisberger U., Trajectory surface hopping within linear response time-dependent density-functional theory. *Phys. Rev. Lett.,* **98** (2007), 023001.

[25] Zheng Q., Chu W., Zhao C., Zhang L., Guo H., Wang Y., Jiang X. and Zhao J., Ab initio nonadiabatic molecular dynamics investigations on the excited carriers in condensed matter systems. *WIREs Comput. Mol. Sci.,* **9** (2019), e1411.

[26] Akimov A.V. and Prezhdo O.V., The PYXAID program for non-adiabatic molecular dynamics in condensed matter systems. *J. Chem. Theory Comput.,* **9** (2013), 4959–4972.

[27] Akimov A.V., Libra: an open-source "methodology discovery" library for quantum and classical dynamics in condensed matter systems. *J. Comput. Chem.,* **37** (2016), 1626–1649.

[28] Barbatti M., Ruckenbauer M., Plasser F., Pittner J., Granucci G., Persico M. and Lischka H., Newton-X: a surface-hopping program for nonadiabatic molecular dynamics. *WIREs Comput. Mol. Sci.,* **4** (2014), 26–33.

[29] Malone W., Nebgen B., White A., Zhang Y., Song H., Bjorgaard J.A., Sifain A.E., Rodriguez-Hernandez B., Freixas V.M., Fernandez-Alberti S., Roitberg A.E., Nelson T.R. and Tretiak S., NEXMD software package for nonadiabatic excited state molecular dynamics simulations. *J. Chem. Theory Comput.,* **16** (2020), 5771–5783.

[30] Mai S., Marquetand P. and González L., Nonadiabatic dynamics: the SHARC approach. *WIREs Comput. Mol. Sci.,* **8** (2018), e1370.

[31] Du L. and Lan Z., An on-the-fly surface-hopping program JADE for nonadiabatic molecular dynamics of polyatomic systems: implementation and applications. *J. Chem. Theory Comput.,* **11** (2015), 1360–1374.

[32] Humeniuk A. and Mitrić R., DFTBaby: a software package for non-adiabatic molecular dynamics simulations based on long-range corrected tight-binding TD-DFT(B). *Comput. Phys. Commun.,* **221** (2017), 174–202.

[33] Dong J., Qiu J., Bai X., Wang Z., Xiao B. and Wang L., SPADE 1.0: a simulation package for non-adiabatic dynamics in extended systems. *J. Chem. Theory Comput.,* **21** (2025), 3300–3320.

[34] Tully J.C., Molecular dynamics with electronic transitions. *J. Chem. Phys.,* **93** (1990), 1061–1071.

[35] Prezhdo O.V. and Rossky P.J., Evaluation of quantum transition rates from quantum-classical molecular dynamics simulations. *J. Chem. Phys.,* **107** (1997), 5863–5878.

[36] Subotnik J.E., Jain A., Landry B., Petit A., Ouyang W. and Bellonzi N., Understanding the surface hopping view of electronic transitions and decoherence. *Annu. Rev. Phys. Chem.,* **67** (2016), 387–417.

[37] Huang L., Shi Z. and Wang L., Detailed complementary consistency: wave function tells particle how to hop, particle tells wave function how to collapse. *J. Phys. Chem. Lett.,* **15** (2024), 6771–6781.

[38] Bittner E.R. and Rossky P.J., Quantum decoherence in mixed quantum-classical systems: nonadiabatic processes. *J. Chem. Phys.,* **103** (1995), 8130–8143.

[39] Bedard-Hearn M.J., Larsen R.E. and Schwartz B.J., Mean-field dynamics with stochastic decoherence (MF-SD): a new algorithm for nonadiabatic mixed quantum/classical molecular-dynamics simulations with nuclear-induced decoherence. *J. Chem. Phys.,* **123** (2005), 234106.

[40] Jaeger H.M., Fischer S. and Prezhdo O.V., Decoherence-induced surface hopping. *J. Chem. Phys.,* **137** (2012), 22A545.

[41] Xu J. and Wang L., Branching corrected surface hopping: resetting wavefunction coefficients based on judgement of wave packet reflection. *J. Chem. Phys.,* **150** (2019), 164101.

[42] Xu J. and Wang L., Branching corrected mean field method for nonadiabatic dynamics. *J. Phys. Chem. Lett.,* **11** (2020), 8283–8291.

[43] Martens C.C., Surface hopping by consensus. *J. Phys. Chem. Lett.,* **7** (2016), 2610–2615.

[44] Barbatti M., Nonadiabatic dynamics with trajectory surface hopping method. *WIREs Comput. Mol. Sci.,* **1** (2011), 620–633.

[45] Schwartz B.J., Bittner E.R., Prezhdo O.V. and Rossky P.J., Quantum decoherence and the isotope effect in condensed phase nonadiabatic molecular dynamics simulations. *J. Chem. Phys.,* **104** (1996), 5942–5955.

[46] Granucci G. and Persico M., Critical appraisal of the fewest switches algorithm for surface hopping. *J. Chem. Phys.,* **126** (2007), 134114.

[47] Subotnik J.E. and Shenvi N., A new approach to decoherence and momentum rescaling in the surface hopping algorithm. *J. Chem. Phys.,* **134** (2011), 024105.

[48] Shao C., Shi Z., Xu J. and Wang L., Learning decoherence time formulas for surface hopping from quantum dynamics. *J. Phys. Chem. Lett.,* **14** (2023), 7680–7689.

[49] Shao C., Xie R., Shi Z. and Wang L., Learning optimal decoherence time formulas for surface hopping simulation of high-dimensional scattering. *arXiv preprint,* (2025), 2510.19238.

[50] Shenvi N., Subotnik J.E. and Yang W., Phase-corrected surface hopping: correcting the phase evolution of the electronic wavefunction. *J. Chem. Phys.,* **135** (2011), 024101.

[51] Ehrenfest P., Bemerkung über die angenäherte Gültigkeit der klassischen Mechanik innerhalb der Quantenmechanik. *Z. Physik,* **45** (1927), 455–457.

[52] Colbert D.T. and Miller W.H., A novel discrete variable representation for quantum mechanical reactive scattering via the S-matrix Kohn method. *J. Chem. Phys.,* **96** (1992), 1982–1991.

[53] Subotnik J.E., Fewest-switches surface hopping and decoherence in multiple dimensions. *J. Phys. Chem. A,* **115** (2011), 12083–12096.

[54] Shao C., Xu J. and Wang L., Branching and phase corrected surface hopping: a benchmark of nonadiabatic dynamics in multilevel systems. *J. Chem. Phys.,* **154** (2021), 234109.

[55] Ibele L.M. and Curchod B.F.E., A molecular perspective on Tully models for nonadiabatic dynamics. *Phys. Chem. Chem. Phys.,* **22** (2020), 15183–15196.

[56] Zhu C., Restoring electronic coherence/decoherence for a trajectory-based nonadiabatic molecular dynamics. *Sci. Rep.,* **6** (2016), 24198.

[57] Coronado E.A., Xing J. and Miller W.H., Ultrafast non-adiabatic dynamics of systems with multiple surface crossings: a test of the Meyer-Miller Hamiltonian with semiclassical initial value representation methods. *Chem. Phys. Lett.,* **349** (2001), 521–529.

[58] Runeson J.E., On decoherence in surface hopping: the nonadiabaticity threshold. *J. Chem. Phys.,* **163** (2025), 154105.

[59] Wang Z., Dong J., Qiu J. and Wang L., All-atom nonadiabatic dynamics simulation of hybrid graphene nanoribbons based on Wannier analysis and machine learning. *ACS Appl. Mater. Interfaces,* **14** (2022), 22929–22940.

[60] He Y., Li T., Gan Z., Chen Y. and Wang L., Machine learning methods for the electronic Hamiltonian. *Sci. Sin. Chem.,* **55** (2025), 1751–1768.